Ductilization of selective laser melted Ti6Al4V alloy by friction stir processing

Chunjie Huang [a*], Xingchen Yan [b,c*], Lv Zhao [a], Min Liu [b], Wenyou Ma [b], Weibin Wang [d], Jeroen Soete [e], Aude Simar [a]

[a] Institute of Mechanics, Materials and Civil Engineering, UCLouvain, 1348 Louvain-la-Neuve, Belgium

[b] Guangdong Institute of New Materials, 510651 Guangzhou, PR China

[c] ICB UMR 6303, CNRS, Univ. Bourgogne Franche-Comté, UTBM, F-90100 Belfort, France

[d] China FSW Center, 100024 Bejing, PR China

[e] Department of Materials Engineering, KU Leuven, 3001 Heverlee, Belgium

* Corresponding author: C.J. HUANG (hcj880923@gmail.com) and X.C. YAN (xingchen.yan@utbm.fr).

Abstract

The low ductility of Ti6Al4V alloy manufactured by Selective Laser Melting (SLM) adversely impacts the component performance in practical applications. A local post-treatment by Friction Stir Processing (FSP) significantly reduces the porosity and homogenizes the microstructure. This results in an increase in fracture strain from 0.21 after SLM to 0.65 following the FSP post-treatment. The porosity reduction was evidenced by 3D X-ray micro-computed tomography. A fully transformed β microstructure is formed after FSP. This microstructure involves α plates, α colonies, as well as equiaxed dynamically recrystallized α phases inside equiaxed prior-β grains. The deformed microstructure was observed during in-situ tensile test, using scanning electron microscopy, with the aim to unravel the damage mechanisms. In addition to the beneficial effect of initial porosity reduction, the transformed microstructure after FSP bears more damage before failure than the typical α' martensite laths in the as-built SLM samples.

Keywords: Selective laser melting (SLM), Ti6Al4V, friction stir processing (FSP), porosity, ductility

1. Introduction

Selective Laser Melting (SLM), a potentially advanced technology, has a high potential for Additive-Manufacturing (AM) of complex-geometry Ti-based components, with interest in a variety of industrial fields, including aerospace, biomedical and automotive [1-3]. Nevertheless, a growing concern has emerged due to the lower mechanical properties (e.g., a relatively low ductility) of SLMed Ti-alloy parts compared to wrought alloys [4,5], which hinder their industrial implementation. Given that the ductility is highly influenced by material defects and the microstructure, it is necessary to investigate the disadvantages of SLMed Ti-alloys, with regards to, e.g., their porosity

[6,7], anisotropy [4,8], microstructure heterogeneity [9], residual stress [10], inappropriate phase formation [4,5,7,11], etc., in order to come up with a tailored ductilization strategy, using post-treatment of SLMed components. The porosity and the acicular α′ martensite present in the as-built Ti6Al4V parts [6], can act as severe stress raiser and initiate premature cracking before or right after the onset of strain localization, thus leading to a low ductility. Vilaro et al. [4] revealed that both the pore shape and building orientation in AMed Ti6Al4V affected the mechanical properties, and a lower ductility was obtained in the transverse direction than in the longitudinal direction. Xu et al. [9] showed that the low ductility of the as-built parts was caused by the presence of brittle α' martensite laths in columnar prior-β grains, while the lamellar (α + β) microstructures could result in superior mechanical properties. Leuders et al. [10] showed that decreasing porosity avoided early crack initiation under high frequency cyclic loading and was more beneficial than microstructural changes in terms of fatigue enhancement.

Given the high advantages of reducing the pre-existing porosity and tailoring the microstructure for improving the mechanical properties of SLMed Ti6Al4V alloy, a variety of thermo-mechanical post-treatments have emerged. Post Heat-Treatment (HT) has proven to be useful for obtaining high strength or high ductility of SLMed Ti6Al4V parts. However, a suitable HT condition must be carefully elaborated to meet the particular applications. For instance, Kasperovich et al. [5] and Yan et al. [7] used different HT to modify SLMed Ti6Al4V samples, and showed that appropriate conditions (700 °C for 1 h and 900 °C for 2 h, respectively) could slightly reduce porosity while strongly modify the microstructure, resulting in an improvement of the material ductility. Vrancken et al. [11] applied a HT at 850 °C below the β-transus temperature (995 °C) to produce an optimal microstructure (lamellar α + β), and showed an increase in elongation at fracture from 7.4 % to 12.8 %.

Hot Isotactic Pressing (HIP) has been widely used for eliminating the internal porosity of SLMed Ti6Al4V parts due to the combined effects of high temperature and high pressure. This process is commonly aims at fatigue life improvement by the suppression of large pores [12]. The quantitative analysis in pore size after HIP has been performed by 3D X-ray Computed Tomography (XCT). Leuders et al. [10] reported that there was no residual porosity detected after HIP treatment in XCT dataset with an isotropic voxel size of 22 µm. Persenot et al. [12,13] stated that samples became free of pores after HIP treatment, in XCT scans with voxel size of 4 µm. Furthermore, Benedetti et al. [14] demonstrated that HIP increased the ductility of SLMed parts, due to a significant reduction in porosity and appropriate microstructure of lamellar α + β. However, the application of HIP also has disadvantages, for instance the increase in grain size [10], the decrease in yield strength and ultimate tensile strength [12], and the remaining anisotropy in ductility [8].

Considering the post-HT or HIP current solutions, new post-treatment processes need to be developed, which improve the material ductility, while limiting the loss in strength and generating a homogeneous microstructure.

Friction Stir Processing (FSP), which is derived from the solid-state welding process of Friction Stir Welding (FSW) has been widely used to locally modify the microstructure as well as the mechanical properties of metallic

materials [15]. FSP is an effective technique for ductilization of aluminum alloys due to porosity reduction, microstructure homogenization, redistribution and size reduction of iron rich second phase particles [16-18]. With the development of new tool materials in the past few years, a growing interest in Friction Stir Processing of Ti6Al4V alloy has emerged [19]. The peak temperatures in the Stir Zone (SZ) strongly depend on the tool geometry, FSP processing parameters, as well as plunge depth. Thus, the temperature in the SZ above or below β-transus during FSP significantly influences its microstructure, resulting in either fine equiaxed prior-β grains decorated by grain boundary α with lamellar colonies α + β inside or bimodal microstructure composed of lamellar α + β [20].

Recently, colleagues at UCLouvain J.G.Santos Macias et al. [21], have applied FSP on SLMed AlSi10Mg alloy and quantitatively assessed the porosity elimination, the microstructural modification and the fatigue life enhancement. However, to the best of the authors' knowledge, evidence for the ductility improvement in SLMed Ti6Al4V alloy by FSP has not been reported in literature. The fracture mechanisms in SLMed Ti6Al4V alloy are related to the phase composition [2], the initial porosity sizes, and their spatial distribution [7]. The main aim of our work is therefore to compare the porosity, the microstructure, and the mechanical properties (both strength and ductility) of SLMed Ti6Al4V before and after FSP.

2. Materials and Experimental methods

2.1 Powder

In this study, the powder used for SLM is provided by EOS company. The Ti6Al4V powder has an extra-low-interstitial grade and is processed by plasma atomization. As shown in Fig. 1, the particles in the powder have spherical shape (Fig. 1b). A sieved particle size fraction between 21.2 µm (d_{10}) and 51.5 µm (d_{90}) was obtained by a laser diffraction measurement (Mastersizer, 2000, Malvern Instruments Ltd., UK), as provided in the inset table of Fig. 1a. Half of the powder volume has a size larger than 33.8 µm (d_{50}). When observing the cross-sectional morphology after etching (see Fig. 1c), it can be seen that the acicular martensitic phase exists in a pore-free structure. The morphology and microstructure of the Ti6Al4V powder were observed using a Scanning Electron Microscope (SEM, FEI Nova NanoSEM 450), operated at acceleration voltage of 15 kV. According to the supplier, the oxygen content in solid solution is lower than 1300 ppm, which is well below the limit imposed by the aeronautical industry for this material (2000 ppm).

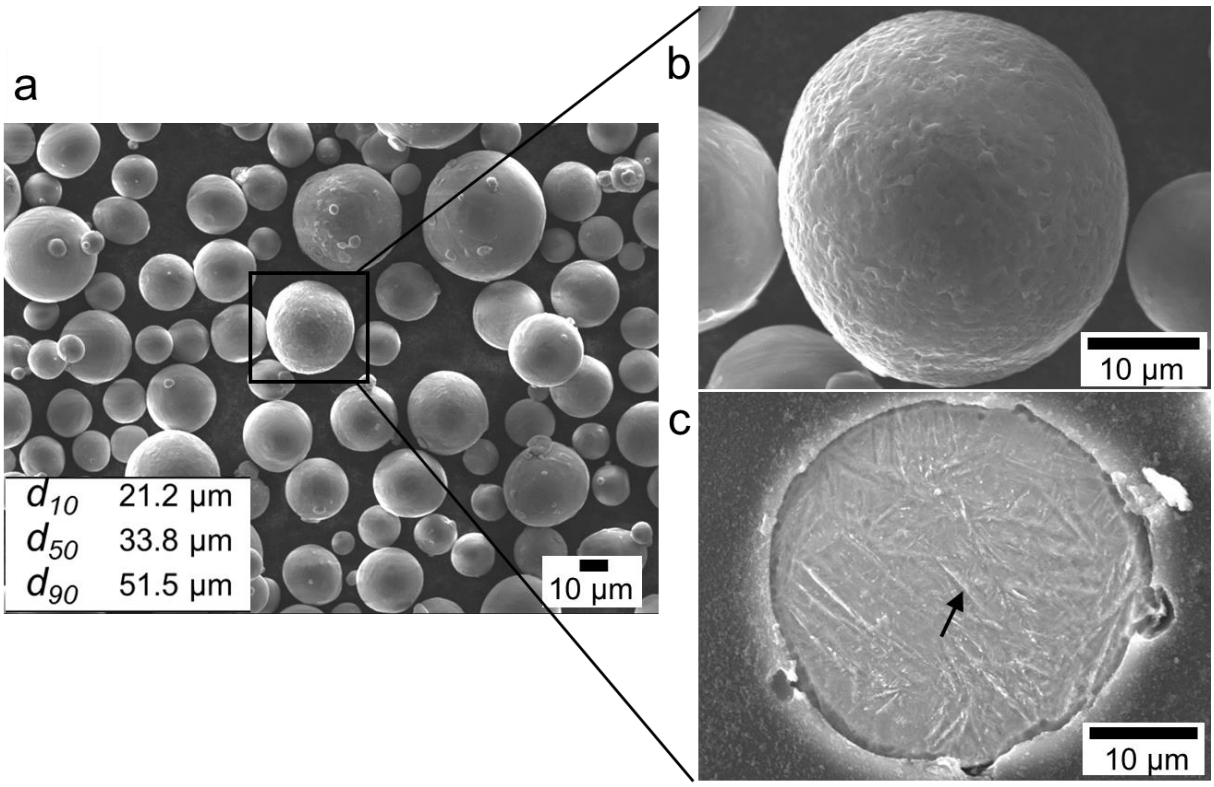

Figure 1. Scanning electron microscopic images of the Ti6Al4V powder. a. at a low-magnification. b. at a high-magnification and c. cross-sectional morphology.

2.1 SLM and FSP

In this study, the Ti6Al4V plates (60×40×3 mm^3) were manufactured by selective laser melting using a commercial EOS M290 machine (EOS, Germany) equipped with a Yb-fiber laser of a wavelength of 1064 nm and maximum power of 400 W. A high purity argon atmosphere flow was used to ensure a low oxygen content during building. Different laser powers (230-280 W) and scanning speeds (800-1400 mm/s) were tested in a preliminary study, reducing porosity as much as possible in the produced parts. The spot diameter, layer thickness and hatch distance were fixed at 100 µm, 50 µm and 50 µm, respectively. The volume fraction of voids was evaluated from 10 optical micrographs using the Image J software (NIH Image, Software, USA). Based on this preliminary study, the laser power was fixed at 280 W and the scan speed fixed at 1200 mm/s. Regarding the laser beam scanning strategy, a rotation of 67 ° around the direction of the laser beam path was conducted for each new layer, see Fig. 2a,

The SLMed Ti6Al4V plates were then friction stir processed perpendicularly to the building direction using a commercial Friction Stir Welding machine (FSW-3LM-020, Beijing FSW Technology Co., Ltd., PR China). A single pass was performed using a traverse speed of 75 mm/min and two different rotational speeds of 350 and 400 rpm, as optimized in a previous study [22]. The schematic diagram of FSP is illustrated in Fig. 2b. The FSP tool (WHTOOL) was made of tungsten and rhenium (W-Re) alloy, and was composed of a 15 mm diameter scrolled shoulder and a 2.5 mm long threaded conical pin. During FSP, the tilt angle with respect to Z-axis was 2.5 °. Argon was continuously supplied to prevent material oxidation. After FSP, Electrical Discharge Machining (EDM) cutting equipment was

used to extract tensile samples from the FSPed stir zone (see Figs. 2c and 2d). The same geometry and dimension were used for the SLMed and FSPed tensile specimens.

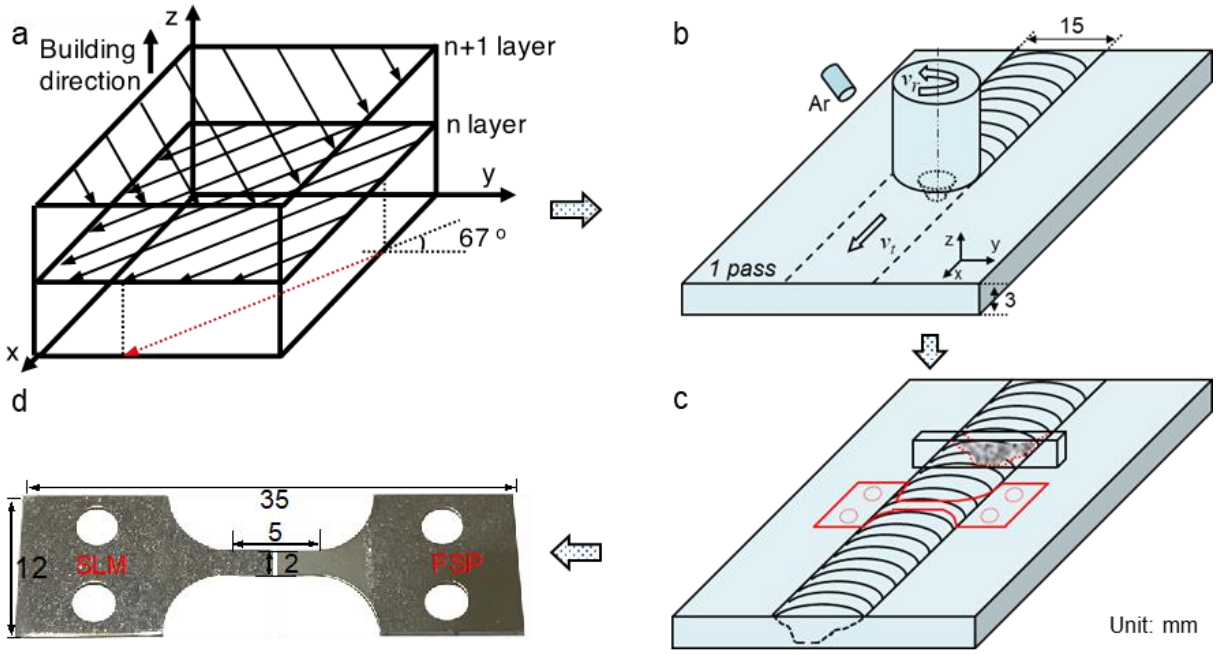

Figure 2. Friction stir processing (FSP) on Ti-6Al-4V plate processed by selective laser melting (SLM). a. Schematic diagram of SLM scanning strategy. b. Schematic diagram of FSP. c. Locations of the extracted tensile and microstructural observation samples. d. Dimension of tensile sample (left: SLM sample, right: FSP sample).

2.3 Microstructure characterization

The microstructural characterization of SLMed plate and the FSP stir zone was carried out by Opto-digital Microscopy (OM, Olympus AX70) and Electron Backscattered Diffraction (EBSD) using a TSL orientation imaging microscope system mounted on a FEI-Nova NanoSEM 450 SEM. Cross-sectioning of a plane perpendicular to FSP direction (see Fig. 2c) was performed by EDM and prepared by standard metallographic procedures. The polished cross-section was chemically etched using Kroll reagent solution (consisted in 92 ml H_2O, 6 ml HNO_3 and 2 ml HF) for 20 seconds. In order to evaluate the microstructure heterogeneity and select between the two FSP rotational speeds, microhardness map was obtained on FSP cross-section using a micro-indentation tester (Emco Test Durascan) with a load of 500 g and a loading time of 10 s.

The spatial distribution of porosity was examined with a High Resolution microfocus X-ray Computed Tomography (HR-microCT), using a Phoenix Nanotom S 180kV µCT system (General Electric). A set of samples (2×3×3 mm) were extracted from the SLMed plate and the FSP stir zone, respectively, and were scanned with an isotropic voxel size of 2 µm, and with 0.5 mm thick copper and aluminum filters installed. The post-processing of the HR-microCT datasets was carried out in the AVIZO 9.7 software. Objects smaller than 3 voxels were filtered out in order to exclude noise from the analysis. Thus, the smallest pores that can be detected have an equivalent diameter of 3.6 µm.

2.4 In-situ tensile testing

Uniaxial tensile tests were performed to evaluate the strength and the fracture strain of both the SLMed and the FSPed samples. The loading rate was set to 0.1 mm/min. The engineering stress as a function of global extension was plotted. The sample geometry is provided in Fig. 2d. One of the sample surfaces was polished and etched in order to monitor the microstructural deformation during loading. Two tests for each material were performed in-situ inside the SEM (ZEISS FEGSEM Ultra 55) using a micro-tensile equipment (Gatan micro-test tensile stage). The elongation at fracture was calculated using a SEM images obtained at initial and final fracture stages. After failure, the crack surface as well as the damage at mid-thickness plane were examined with SEM.

3. Results

3.1 Macrographs and phase characterization

3.1.1 As-built SLM sample

Typical OM microstructure from the top view of the SLMed Ti6Al4V sample is shown in Fig. 3a. Pores are clearly present, and originate from the insufficient overlap of neighboring scan tracks. The side view in Fig. 3b (YZ plane) reveals that long oriented columnar prior-β grains grow up to several millimeters in length. This growth was shown previously to be epitaxial from one melt pool to the one above [11]. These prior-β grains are decorated by grain boundary α phase (called GBα in Figs. 3a and 3b) and composed of a fully acicular α' martensite (β→α') due to the high cooling rate (10^3-10^5 K/s) and the high temperature gradient (10^4-10^5 K/cm) during SLM [9]. The growth direction of columnar prior-β grains is opposite to the direction of heat flow as previously reported [23], which can also be inferred from the columnar shape of prior-β grains that extend along the building direction (Z-axis). The average width of the columnar prior-β grains is typically 100 µm, which corresponds well to the laser spot diameter. In addition, the α′ martensite laths initially nucleate at ~45° to the columnar prior-β grain boundaries and then grow within the parent β grains, as shown in Fig. 3b. The average microhardness measured in the XY plane is 408 $HV_{0.5}$.

In order to better reveal the α′ martensite laths inside the columnar grains, EBSD was used to investigate their morphology and substructure on the YZ plane, as shown in Figs. 3c-3d. At a low magnification, numerous acicular structures with different sizes are highlighted, which result from the displacive phase transformation from *BCC*-β to *HCP*-α′ upon cooling already described in literature [23]. Indeed, the cooling rate during SLM is much higher than the critical cooling rate (about 410 °C/s) required for the martensite formation. The primary α′ martensite laths can also be observed inside the prior-β grains in Fig. 3c. Aiming to further clarify the morphologies of the α′ martensite laths inside the β grains, an inverse pole figure (IPF) map at higher magnification is presented in Fig. 3d, which shows that the α′ martensite laths are either parallel or perpendicular to each other. The lath width of the α′ martensite laths and the misorientation angle distribution (corresponding to Fig. 3c) are shown in Figs. 3e and 3f, respectively. The average lath (grain) width is about 1 µm and involves mostly (91 %) high-angle grain boundaries (HAGBs), resulting from the complex thermal cycles and high cooling rates of the SLM process.

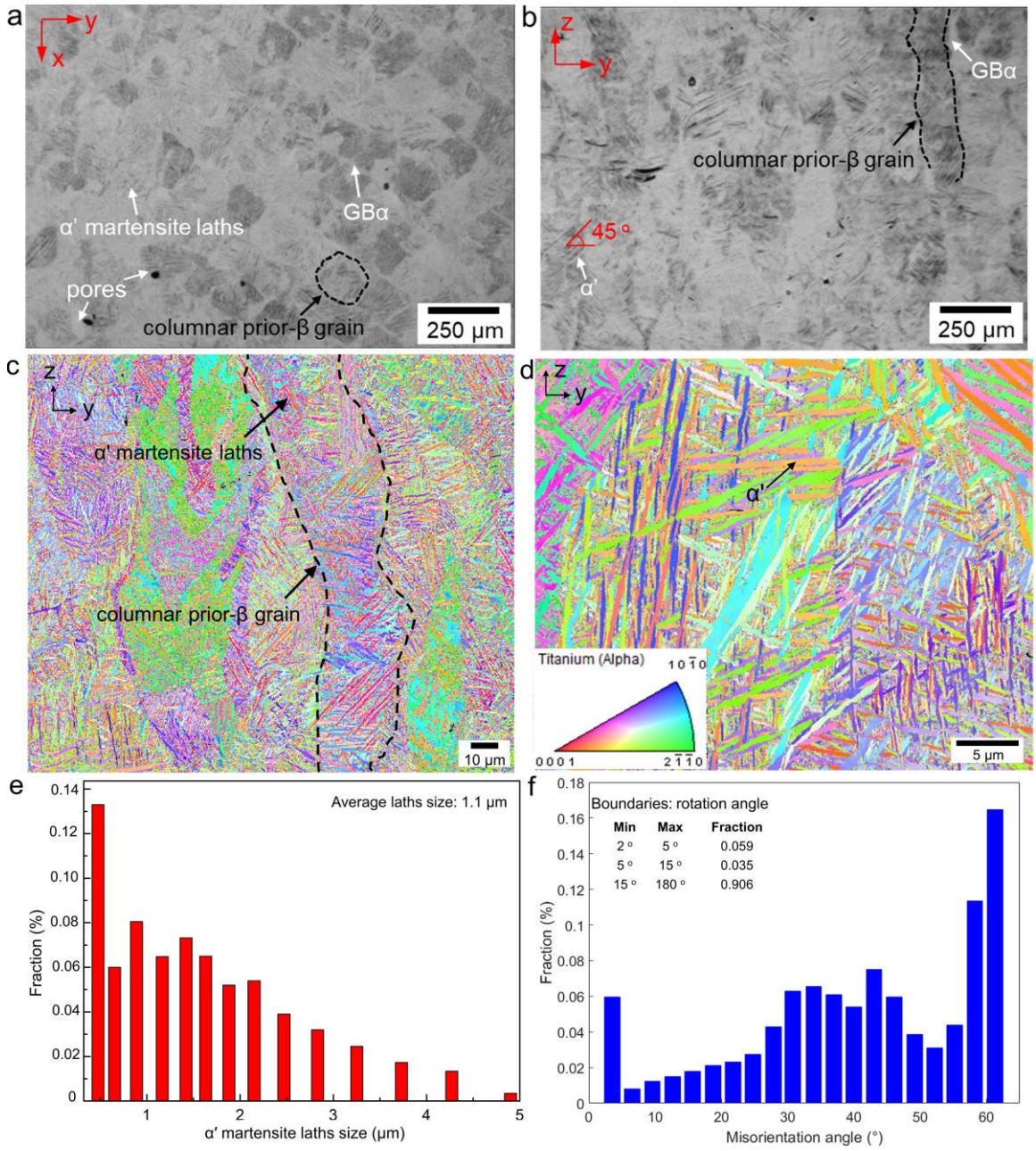

Figure 3. Microstructures of SLMed Ti6Al4V alloy. a and b. OM images of top (XY plane, see Fig. 2a) and cross-section views (YZ plane), respectively. c. EBSD IPF map, where red, green, and blue colors indicate {1010}, {0001}, and {2110} grains, respectively. d. IPF map at higher magnification, e. Lath size distribution and f. misorientation angle distribution (both corresponding to Fig. c).

3.1.2 FSPed samples

Processing parameters are the key factors in dictating the microstructure and properties of FSPed Ti-6Al-4V alloy. The material will experience dynamic recrystallization and phase transformation during FSP [22]. Due to the sensitivity of the Ti6Al4V alloy to the processing temperature, a very narrow processing window is considered in this study, also proposed by Mironov et al. [19]. Fig. 4 shows the OM cross-sectional macrograph and microhardness distribution of SLMed Ti6Al4V alloy obtained at two different rotational speeds: 350 and 400 rpm. The FSP processing direction corresponds to the X-axis direction of SLM. RS and AS stand for retreating and advancing sides

of the tool, respectively. It is clearly seen that both processed zones present the classical basin-shape [19,20]. An abrupt and visible transition between the SZ and the as-built zone is observed, as denoted by the white dashed lines in Figs. 4a and 4c. FSPed Ti6Al4V presents extremely narrow thermo-mechanically affected zones [19,22]. As expected and noted in Fig. 4b, the unaffected zone shows similar microhardness as the SLM material (408 $HV_{0.5}$). Moreover, large inhomogeneities probably due to insufficient material flow under a low rotational speed are observed in Fig. 4a. In addition, the microhardness varies along the thickness direction (see Fig. 4b). The variation in microhardness is expected to be the result of an inhomogeneous microstructure distribution. A microstructure inhomogeneity along the thickness was also reported by Yoon et al. [24] with a similar rotational speed of 300 rpm. At a higher rotational speed which involves a larger heat input, a more homogeneous microstructure and microhardness distribution are obtained, as shown in Figs. 4c and 4d. In what follows, only the FSP samples, with a rotational speed of 400 rpm will be further analyzed and referred to as "FSPed sample". The microstructural analysis and tensile tests were extracted from the SZ of the FSPed sample identified by the white rectangle in Fig. 4c.

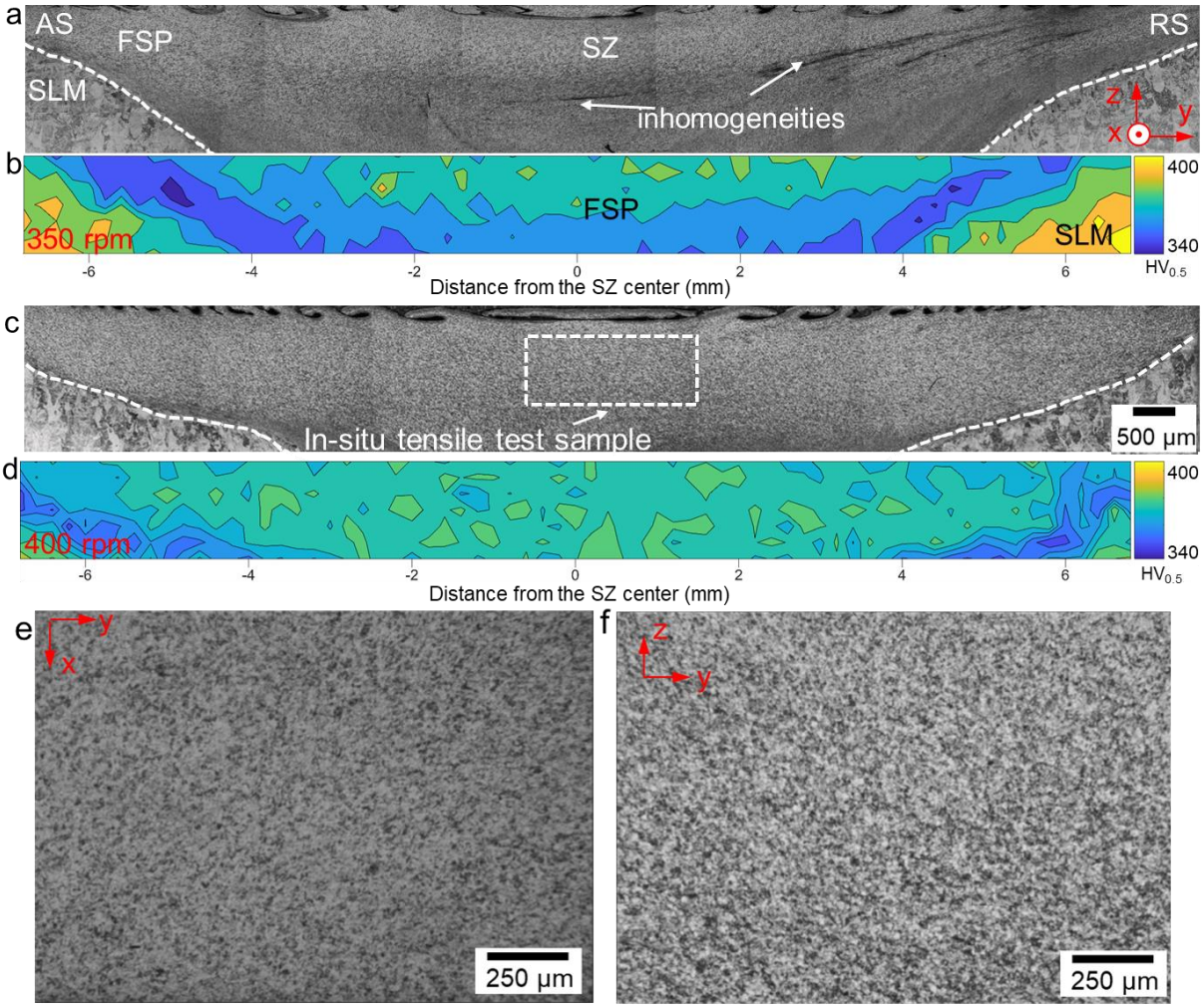

Figure 4. a and c. Optical microscopy (OM) observations of SLMed Ti6Al4V alloy after FSP at the rotation speeds of 350 and 400 rpm. b and d. Microhardness distributions corresponding to a and c. The rectangle in (c) shows the location of tensile sample gauge

section. e and f. OM images of top view and cross-section views of the stir zone for the sample performed at a rotational speed equal to 400 rpm, respectively. AS = advancing side, RS = retreating side.

Figs. 4e and 4f present optical micrographs of the FSPed sample, taken at the same magnification as in Figs. 3a and 3b. They show a completely mixed microstructure composed of ultrafine grains after FSP, incorporating homogeneously distributed α phase (white contrast) and β phase (grey contrast), while the dominating large columnar prior-β grains in the SLMed sample are no longer visible. This microstructural evolution results from the complex thermo-mechanical effects involving the combined actions of heat transfer and material flow during FSP [20]. The observations of the top and side views (Figs. 4e and 4f, respectively) manifest a homogeneous microstructure, which will now be further explored by EBSD.

Fig. 5 provides an EBSD analysis of the 400 rpm FSPed sample. The microstructure morphology, grain boundary map and IPF map of the α-phase are shown at various resolutions. Comparing the EBSD maps of the SLMed Ti6Al4V alloys before (Fig. 3d) and after (Fig. 5d) FSP, it is observed that the acicular α′ martensite laths contained in columnar prior-β grains in the SLMed sample are converted. After FSP, the large columnar prior-β grains are no longer present after cooling from the above β-transus temperature (compare between Figs. 5a-5b and Figs. 3a-3d). The columnar prior-β grains of the SLMed sample are substituted by the much smaller equiaxed prior-β grains (~2.9 µm) in the SZ of the FSPed sample, indicating that the SZ has experienced dynamic recrystallization (DRX) during FSP, as classically reported in literature [25]. During FSP of Ti6Al4V alloys, the temperature in the SZ generally exceeds the β-transus temperature, thus resulting in a fully transformed β structure through β→α + β phase transformation from the single β phase during cooling. The lamellar microstructure inside the equiaxed prior-β grains involves α plates (about 0.2 µm in width) and extremely fine α colonies, see Figs. 5e and 5f. These colonies have a size of about 0.6 µm and are present in between α and β lamellar (as marked by circles in Figs. 5e). The prior-β grains are surrounded by the GBα, as shown under both the low and high magnifications in Figs. 5a and 5c, respectively. In addition, the phase map in Fig. 5g confirms a clear distribution of β phase within the α colonies. The aforementioned microstructure confirms that the SLMed Ti6Al4V sample was heated up above the β-transus temperature during FSP.

In addition, as a consequence of the DRX, which results from the intense plastic deformation and frictional heating, very fine (typical size of 0.3 µm) and equiaxed α phase is present inside the β grains (see Figs. 5e and 5f). In turn, the existence of a large amount of equiaxed α phase confirms the DRX process in the SZ [26]. The distribution of misorientation angles is presented in Fig. 5h. It shows a higher ratio of HAGBs (92 %) compared to the SLMed material (Figs.3f). FSP turns out to be a promising post-treatment process on the SLMed Ti6Al4V alloy to produce an ultrafine-grained structure.

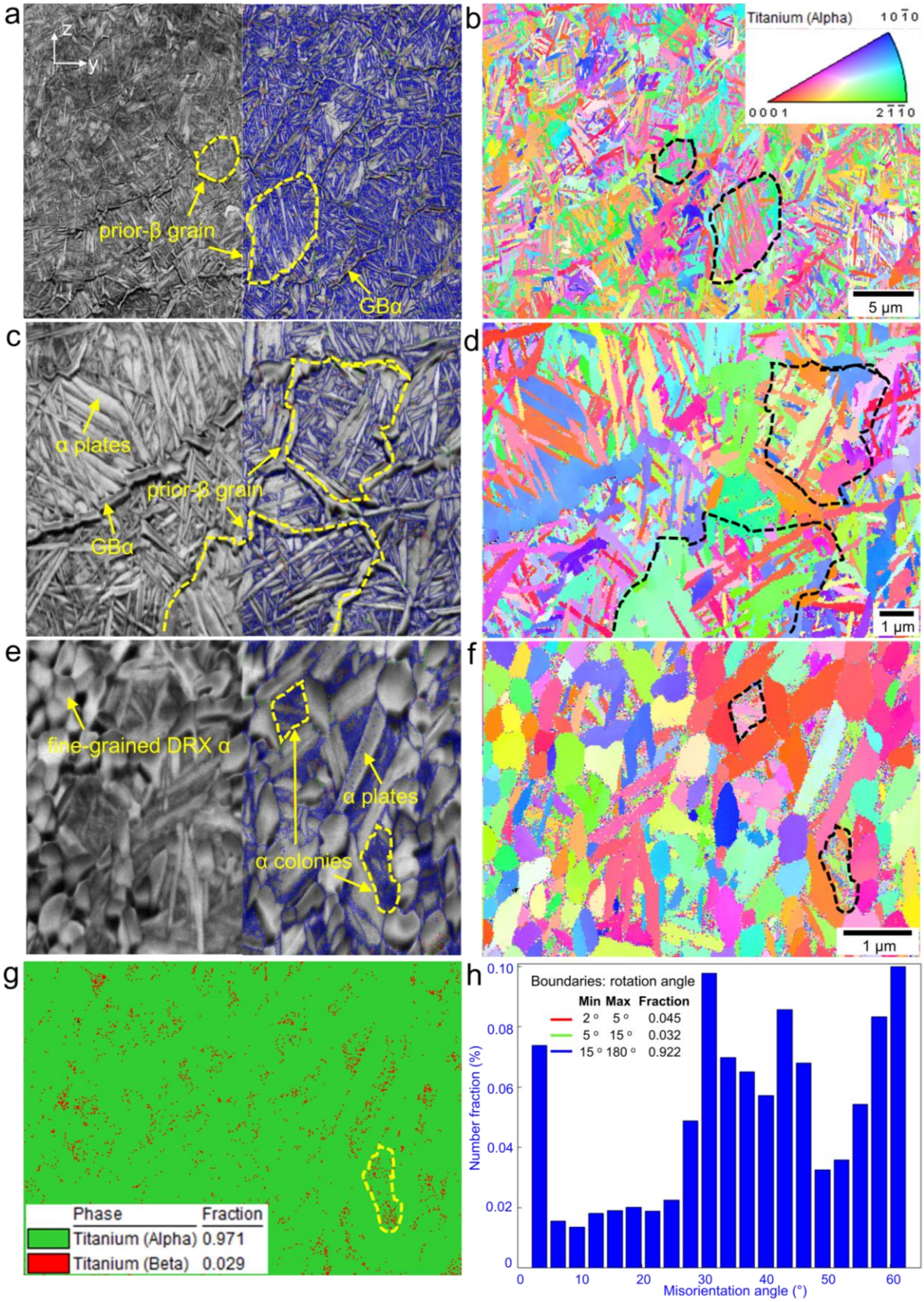

Figure 5. EBSD analysis of FSPed sample at different magnifications. a, c and e. Microstructure morphology (left) and grain boundary map (GB, right). b, d and f. Corresponding IPF map images. g, EBSD phase map corresponding to the same location as e and f,

showing in green the α phase and in red the β phase, the dashed line highlights the α colony. h. Distribution of misorientation angle corresponding to f. Note that the red, green and blue bars in Fig. 5h represent different GB misorientation angles in GB maps of a, c and e.

3.2 Porosity analysis

In as-built SLM samples, pores are generally present due to incomplete remelting of the previous layer when building the actual one [4,7,28-30]. It is well recognized that the pores can result in local stress concentration, thus giving rise to degraded mechanical properties. The ductile fracture develops from micro-void nucleation, steady growth, and final coalescence with neighboring voids [27]. Given the detrimental effects of porosity on the mechanical behavior of the materials, as emphasized in previous studies [4,7,28-30], an investigation by HR-microCT is performed in order to explore how FSP modifies the porosity in the SLMed Ti6Al4V. The overview of the pores in the as-built sample is scanned in Fig. 6a. A void volume fraction of 0.02 % is obtained in the scanned sample. The colors in the volume rendering of the pores represent the pore sizes, as illustrated in the color legend in Fig. 6a. The size distribution of the pores is provided in Fig. 6c, indicating that the SLMed sample contains some very large pores (up to 43.8 µm). In addition, the smaller pores (below 3 µm) are characterized using 2D SEM images. It is evidenced that they are quite numerous but cannot be captured by the 3D tomography due to the limited resolution.

In the HR-microCT sample extracted from the SZ of FSP, no pores are detected at an isotropic voxel size of 2 µm, as shown in Fig. 6b. This implies that the large pores are reduced in size or eliminated due to the thermomechanical effect of FSP [16,18]. Considering the voxel size and the filtering strategy, the detection ability expressed in equivalent pore diameter is 3.6 µm. It means that if pores still exist after FSP, their equivalent diameter should be smaller than 3.6 µm, note that the maximum pore size in the as-built materials is 43.8 µm. It is worth mentioning that even with high magnification SEM observations, no pores are found in the SZ, as shown in Fig. 6d. In that respect, it can be concluded that one single FSP pass has the ability to significantly reduce or even eliminate porosity in the SLMed material.

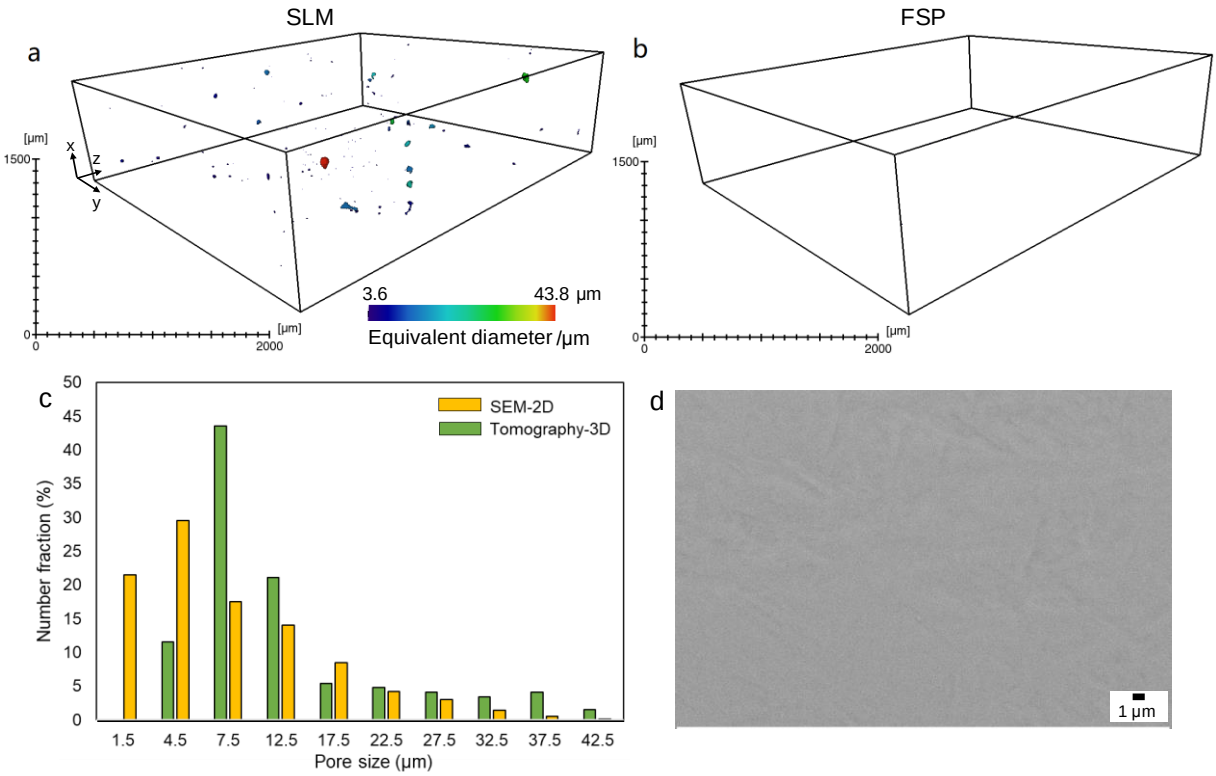

Figure 6. 3D X-ray microtomography perspectives of pore distribution for the Ti6Al4V samples. a. SLMed sample and b. FSPed sample. The large pore size can be inferred from the red color. c. Size distribution of the pores in SLMed sample based on the 3D X-ray microtomography data and SEM images. d. SEM image from SZ of the FSPed samples at high magnification showing no pores.

3.3. Mechanical tests

3.3.1 Mechanical strength and fracture strain

In order to compare the deformation and fracture mechanisms between the SLMed and the FSPed Ti6Al4V samples, in-situ tensile tests were performed in the SEM. The loading was interrupted during tensile testing in order to take SEM micrographs at different deformation stages (see Fig. 7a). The true fracture strain (ε_f) is calculated by Eq. 1, using the initial cross-section area (A_0) and final fracture surface area (A_f) [18]. A_f is measured from the fracture surface of the broken samples (Fig. 7b). The ultimate tensile strength (UTS), true fracture strain and elongation at fracture are provided in Table 1.

$$\varepsilon_f = ln(A_0/A_f) \quad (1)$$

Table 1. Tensile properties of the SLMed and the FSPed Ti6Al4V samples. UTS and ε_f represent the ultimate tensile strength and true fracture strain, respectively. Values in the table are the average of 2 samples, the deviation between the results of the two samples is below 5 %.

Sample	UTS (MPa)	Elongation at fracture (%)	ε_f
SLM	1261	10	0.21
FSP	1085	20	0.65

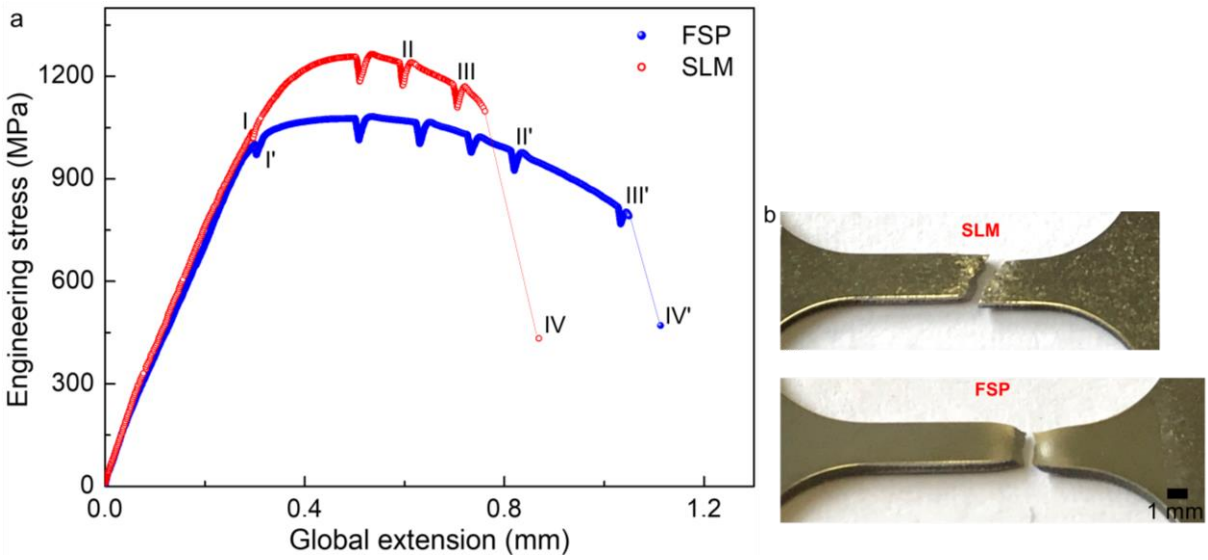

Figure 7. a. Force *vs.* displacement curves of in-situ SEM tensile test, red and blue lines represent SLMed and FSPed samples, respectively. The load drops denote the stress relaxation that occurred when the test was interrupted for observing deformed microstructure. b corresponds to stages IV and IV' in Fig. 7a, i.e. planar view of the fractured samples.

According to tensile properties presented in Table 1, the FSPed sample presents has an average UTS of 1085 MPa, which is about 13.9 % lower than that of the SLMed sample. The fracture strain of the SLMed sample is 0.21, while that of the FSPed sample is greatly improved to 0.65, which represents an improvement of a factor 3 in ductility thanks to this FSP post-treatment. The elongation of fracture, measured on the final broken samples, is improved by a factor 2, from 0.1 to 0.2. It can be summarized that the high strength in the SLMed samples is accompanied by a low ductility, while the FSP post-treatment results in a significantly higher ductility at the expense of only a very slight drop in mechanical strength.

3.3.2 In-situ tensile deformation evolution

Fig. 8 shows the in-situ SEM images at different strain levels of the SLMed and the FSPed Ti6Al4V samples. The four strain levels (see Fig. 7a) selected in the stress-displacement curves, are (I and I') the early stage of plastic deformation, (II and II') the post-necking stage, (III and III') the damage stage, and (IV and IV') the final fracture stage. The corresponding SEM images for the SLMed and FSPed samples are presented in Figs. 8a-d and Figs. 8e-h, respectively. The insets systematically present higher magnification images of the microstructure.

At the global extension of 0.29 mm (Fig. 8a), the SLMed sample presents no visible modification of the microstructure (see Fig. 8a') since limited plastic deformation is involved. In what follows, Fig. 8b (corresponding to a global extension of 0.59 mm) shows irreversible plastic deformation in the form of slip-bands (denoted by red arrows). These slip-bands initiate inside large columnar prior-β grains, as shown in Fig. 8b and the inset Fig. 8b'. After slight necking (Fig. 8c), a global shear band, which crosses the two necks, can be clearly noticed (marked by black arrows in Fig. 8c'). At this stage, some microcracks are identified in Fig. 8c' (identified as i, ii and iii on the inset). These damages are present right along the boundaries between the α′ martensite laths, where the deformation

incompatibility and accumulated dislocations are present. At the final failure stage, as presented in Fig. 8d (and the inset Fig. 8d'), the orientations of microcracks are different in different prior-β grains. The previously observed microcracks are significantly enlarged, and a slant fracture occurs inside the diffuse neck at a global extension of 0.87 mm. The fracture path presents a zigzag feature to accommodate local microcracks which are differently oriented in the damage stage, as indicated by red lines in Fig. 8d.

A completely different microstructure evolution and fracture process is observed during the in-situ loading and monitoring of the FSPed sample. Similar to the loading stage I for the SLMed sample (see Fig. 8a), no microstructural changes can be observed at the loading stage I' for the FSPed sample (see Fig. 8e). At the stage II' (corresponding to a global extension of 0.82 mm), the slip-bands can be barely observed at the lower magnification (×30) (see Fig. 8f). This is due to the deformation of much smaller equiaxed prior β grains in the FSPed sample. At higher magnification, as shown in the inset of Fig. 8f', the elongated GBα and some slip-bands in α lamellar (marked red arrows) can be noticed. This was already observed by Ren et al. [31] in a Ti6Al4V alloy by laser solid forming, where such slip bands were found in α laths. When the FSPed sample was loaded to 1.03 mm (Fig. 8g), the necking becomes more significant. However, no global shear band is present. Some damage is visible (see inset Fig. 8g'), involving microvoids and microcracks along the slip-bands at α phase boundaries. In contrast to the damage in the SLMed sample (see Figs. 8c' and 8d'), the damage observed in the FSPed sample has no preferential orientation. The final failure (stage III') of the FSPed sample occurs at a larger extension with a much more significant section reduction, i.e. a much larger fracture strain. The crack path in the FSPed sample (see Fig. 8h') is almost perpendicular to the loading direction, in contrast to the slant fracture of the SLMed sample. This fracture feature can be related to the fact of the extremely refined microstructure, so the local voids only develop inside the neck instead of crossing the neck to follow the global shear band.

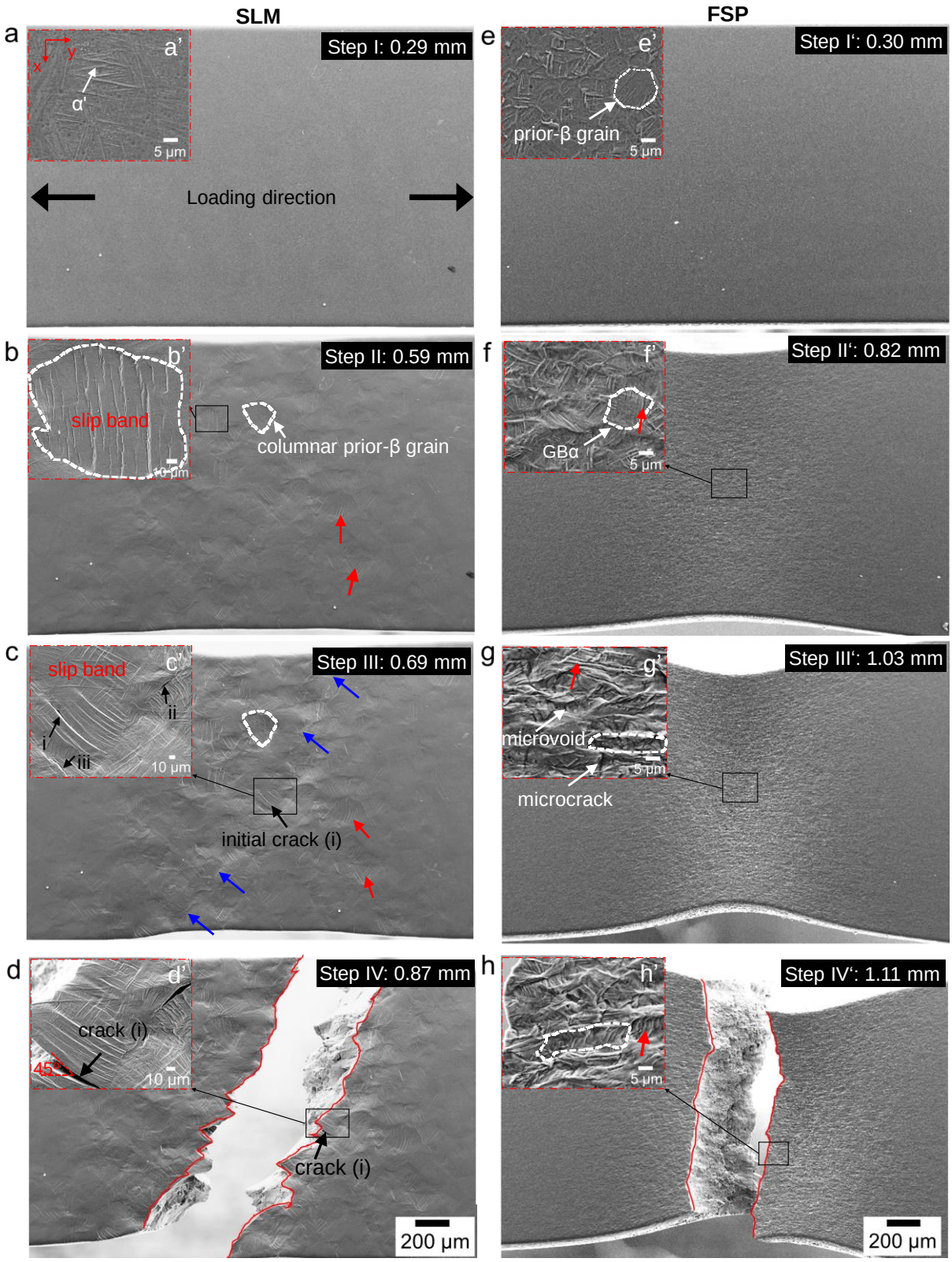

Figure 8. SEM images during in situ tensile testing at different strain levels. Images at the loading stages I-IV and I'-IV' of Fig. 7a are provided in Figs. a-d and Figs. e-h. The inset figures represent the microstructures at high-magnification marked by the black rectangles. Red arrows indicate the slip bands.

3.4 Damage mechanism

3.4.1 Damage near the fracture surface

To further characterize damage mechanisms in both the SLMed and FSPed samples, the fractured specimens are polished to the mid-thickness plane and SEM observations are carried out on this plane. Figs. 9a and 9b present an overview of that mid-thickness plane including the entire necking zone of both the SLMed and the FSPed samples, respectively. According to the observations at higher magnification, the SLMed sample contains both small and large voids at the vicinity of the fracture surface, as presented in Fig. 9c. The large voids, usually distant from the fracture surface, likely correspond to enlarged pre-existing pores that have grown under the plastic deformation, as they are bigger than the pores closer to the fracture surface, where the local strain is expected to be higher. Some of these large voids are coalescing, as can be observed in Fig. 9c. One important feature of these larger voids is that they generally have a large aspect ratio (see Fig. 10), which indicates that their void growth is likely driven by local shear. This feature is in good agreement with the micro-cracks which are present along inclined α' lath boundaries, as observed during the in-situ tensile test and previously presented in Fig. 8c' and 8d'. In regions far away (outside the necking region) from the fracture surface, only pre-existing pores are observed, see Fig. 9e.

For the FSPed sample, the high magnification image of Fig. 9d reveals different shapes and distributions of the voids. The voids are generally spherical, which is in contrast to the elongated shape that has been observed in SLMed sample (Fig. 10). The voids are present both inside the α phase and at the GBα. It is, however, not straightforward to distinguish whether the voids are inside the α plates or at their boundaries due to the large deformation (fracture strain of 0.65, as presented in Table 1). There are no voids observed far away (outside the necking region) from the fracture surface (see Fig. 9f), which partly confirms the result of the 3D HR-microCT and 2D SEM analysis on the porosity of the FSPed sample (see Figs. 6b and d). Excluding the pre-existing pores, it can be seen that the voids are more numerous and larger in the FSPed sample than in the SLMed one, as shown in Fig. 10. This suggests that the FSPed material can tolerate more damage before failure than the SLMed material, which is in good agreement with the significant difference in fracture strain.

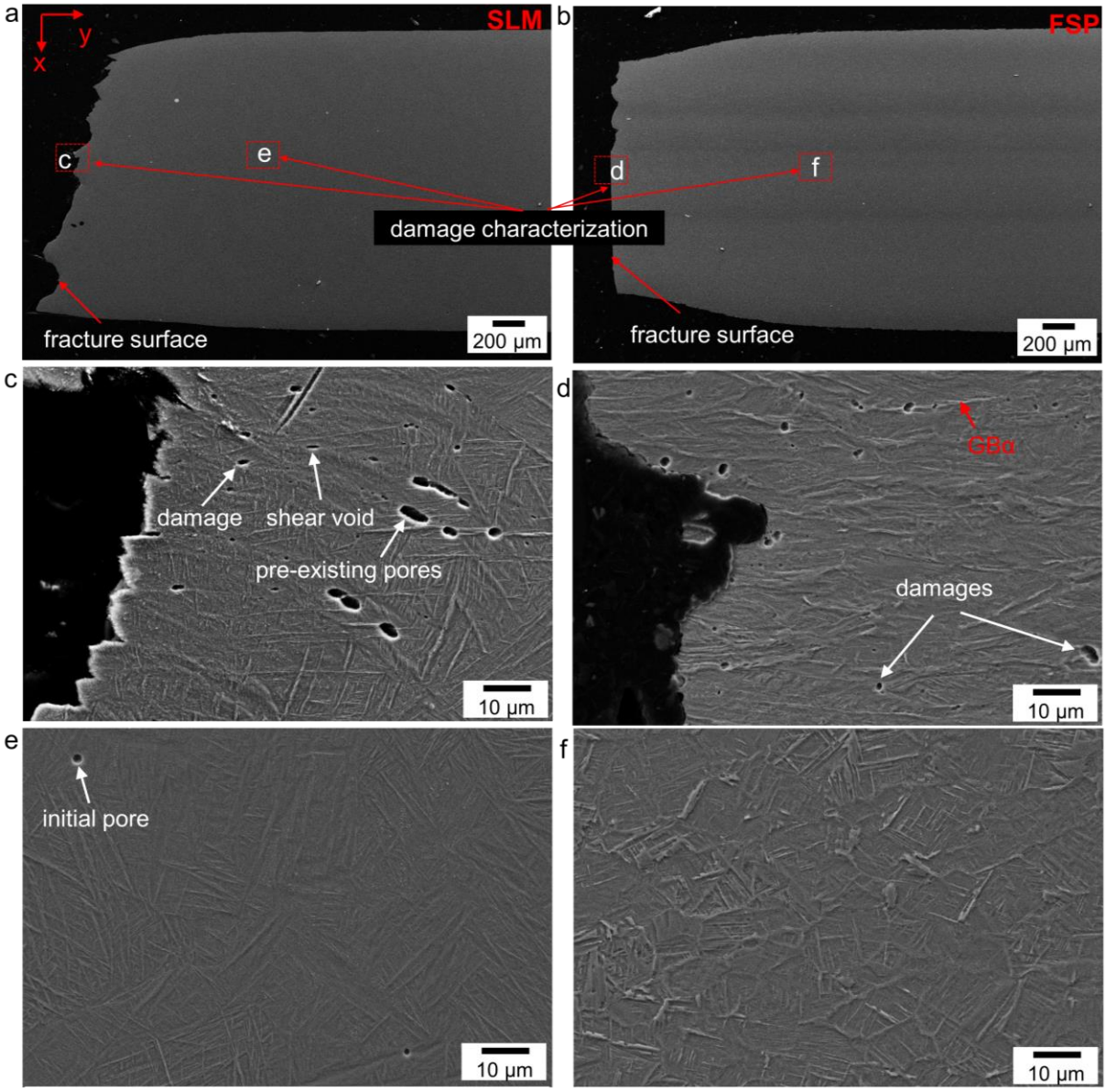

340

341 **Figure 9.** SEM images of polished (to mid-thickness) fractured tensile samples showing the position of the regions where the damage
342 was initiated at different distances from the fracture surface. Overview of the neck zone at mid-thickness plane (a) SLM and (b) FSP
343 providing the location of figures (c-f) that are observed using high magnification.

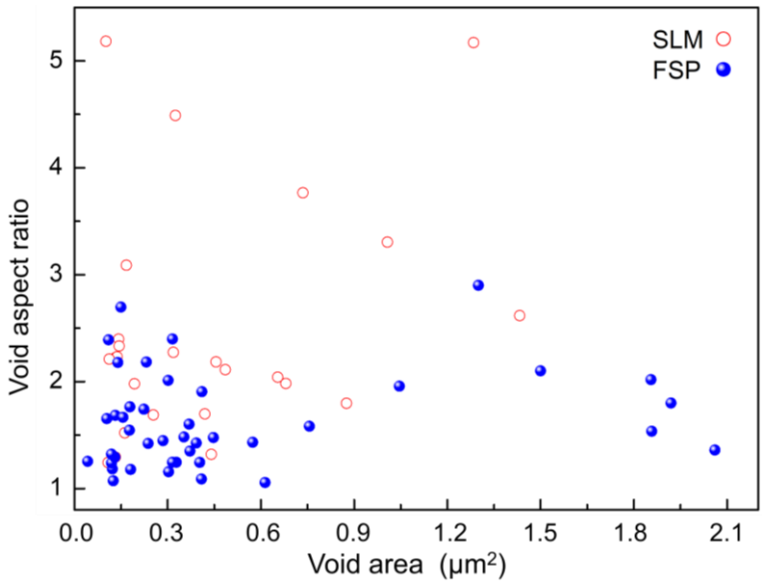

Figure 10. Damage analysis at the vicinity of the fracture surface showing variations in void aspect ratio as a function of void area.

3.4.2 Fractography

In order to further study the fracture mechanism, detailed SEM images of the fracture surface are made. Fig. 11a shows a typical faceted fracture morphology of the SLMed sample. These extensively faceted areas suggest that the crack follows the differently oriented microcracks, which are formed along the α' lath boundaries in the various prior-β grains (previously evidenced in Fig. 8d). At high magnification (see Fig. 11c), shallow sheared dimples are observed at the fracture surface, which correlates well with the elongated voids observed in Fig. 9c. Moreover, some deep voids can be noticed, which likely correspond to pre-existing pores. When compared to the fracture surface of the FSPed sample (see Fig. 11b), the examined fracture surface exhibits a more ductile character with highly teared dimples. Moreover, it is found that the dimples are deeper than that in the as-built material. These teared dimples correspond well to the higher ductility of the FSPed sample.

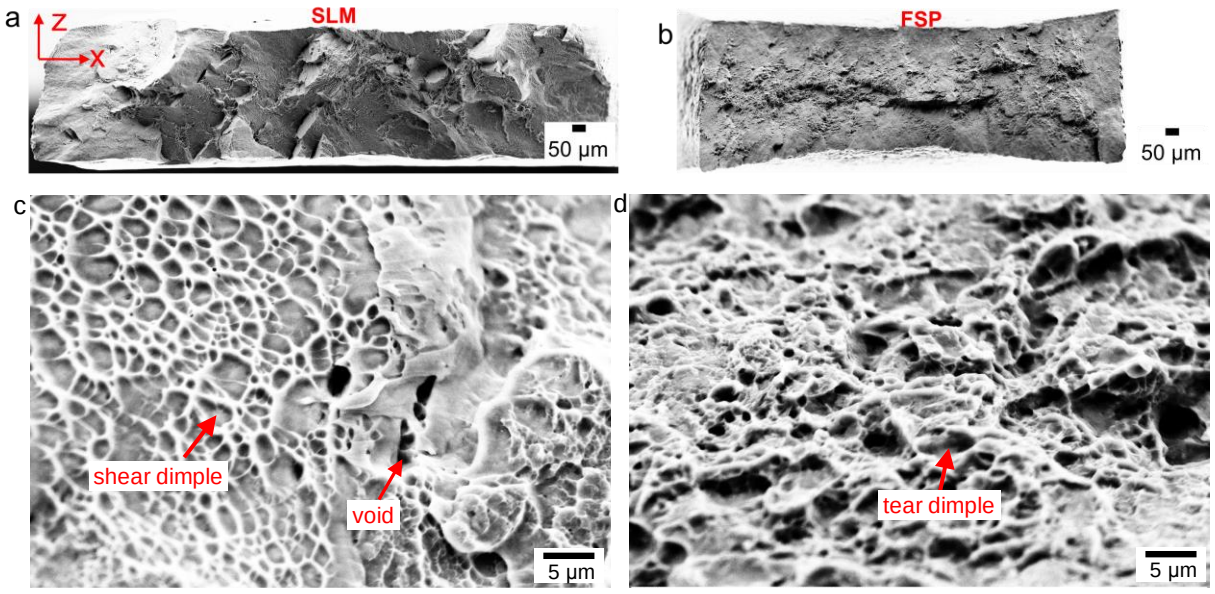

Figure 11. SEM fractographic surfaces: a and c. SLMed sample, and b and d. FSPed sample.

4. Discussion

The low ductility of the SLMed Ti6Al4V alloy originates from various sources e.g. i) the presence of pre-existing large pores [6], ii) the presence of acicular martensite variants and large columnar prior-β grains [32], and iii) residual stresses [10]. Porosity characterization has been addressed in several studies [4-7,10,28-30], which indicate that the typical layered microstructure resulting from the SLM process presents a variety of pore sizes, shapes and distributions. Small spherical pores in the SLMed material are formed due to entrapment of gases originally present in the gas atomized metal powders, while large irregular pores (also observed in Fig. 6a) result from the lack of fusion defects [29]. It is well known that ductile fracture involves void nucleation, growth and coalescence [10,33]. In the case of SLMed materials, damage growth develops early, as pre-existing (large) pores directly grow with the continuous plastic deformation, and then coalesce with other grown pores or newly nucleated voids. As a result, the accumulation of void linkage (see Fig. 9c) will lead to the formation of the microscopic cracks, which propagate until final failure.

With respect to the α′ martensite laths in the SLMed Ti alloy, it has been reported that they can result in a high yield strength (about 1 GPa [6]) and a high UTS (1.24 GPa [7]), but generally involve both a low ductility (total uniform elongation at failure < 10 %[6]) and a high scatter in fracture toughness (16-67 MPa√m [2]). The high strength of the SLMed Ti6Al4V alloy results from the fact that, during the SLM process, the high temperature gradient and rapid cooling rate contribute to the formation of a large number of distorted acicular *HCP*-α′ phases with the presence of internal stresses inside the martensitic laths. In a nutshell, the extensive pores as well as the brittle martensite laths contribute to the significant loss in ductility of SLMed materials.

As shown in Table 2, among the typical post-treatments of SLMed materials, subtransus HT enables a relatively high UTS, while a low elongation at fracture [4,5,10,11]. Supertransus HT allows relieving residual stresses and

increasing ductility, but jointly leads to a significant loss in mechanical strength due to significant microstructure coarsening [4,10,11]. HIP enables reducing porosity and releasing residual stresses but shares the same disadvantages as HT, for instance the UTS reduction [5,8,10]. The post-treatment of FSP has been performed for the first time on SLMed Ti6Al4V alloy in the present work and shows a strong potential in ductilizing SLM as-built material. The beneficial effects of FSP, such as porosity reduction, microstructure modification and grain refinement [16,18] translate into an increase by a factor 3 in ductility while accompanied by a limited reduction of 13.9 % in mechanical strength. The improvement in ductility could be attributed to two main factors: the first one is the reduction of large pores in the as-built material; the second involves the phase change from the brittle α′ martensite laths to the relatively softer α + β phase. The limited decrease in mechanical strength compared to HT or HIP can be related to the finer microstructure driven by the transformed α colonies [20] and dynamic recrystallization [26] during FSP. Indeed, the generated smaller equiaxed prior-β grains can benefit from the strengthening related to size effect (Hall-Petch mechanism [34]). It is worth noting that the FSPed sample (in this work) has a mechanical strength 12% higher than the HIPed sample [5] at a similar (even slightly higher) elongation at fracture. On the other hand, the FSPed sample presents a higher ductility than the HT [4] or HIPed [8,10] samples at a similar mechanical strength. The application of FSP on SLMed Ti6Al4V alloy promotes new investigations on fracture toughness, fatigue resistance as well as fatigue crack propagation rate, so that a complete comparison between HT, HIP and FSP can be established in the future.

Table 2. Comparison of the UTS and elongation at fracture in the SLMed and heat-treated Ti-6Al-4V alloys between the references and the present work.

Refs.	Process and post-treatments	UTS (MPa)		Elongation at fracture (%)	
		LD	TD	LD	TD
[4]	SLM	1206	1166	7.6	1.7
	SLM + 730 °C for 2 h AC	1046	1000	9.5	1.9
	SLM + (950 °C/1 h WQ+ 700 °C/2 h AC)	1036	1040	8.5	7.5
	SLM + (1150 °C/1 h WQ+ 820 °C/2 h AC)	1019	951	8.9	7.9
	WC = water quenching, AC = air cooling; longitudinal direction (LD) and transverse direction (TD)				
[5]	SLM	1051		11.9	
	SLM + 700 °C for 1 h	1115		11.3	
	SLM + (900 °C for 2 h + 700 °C for 1 h)	988		9.5	
	SLM + HIP (920 °C + 100 MPa for 2 h) + (700 °C for 1 h)	**973**		**19.0**	
	FC = furnace cooling, All specimens were after FC				
[8]	SLM	1200		5.1	
	SLM + HIP (920 °C + 103 MPa for 4 h FC)	**1067**		**12.6**	

[10]	SLM	1080	1.6
	SLM + 800 ºC for 2 h	1040	5
	SLM + 1050 ºC for 2 h	945	11.6
	SLM + HIP (920 ºC + 100 MPa for 2 h)	**1005**	**8.3**
	All specimens were after FC.		
[11]	SLM	1267	7.3
	SLM + 540 ºC for 5 h WC	1223	5.4
	SLM + 850 ºC for 2 h FC	1004	12.8
	SLM + 705 ºC for 3 h after AC	1082	9.0
	SLM + 1020 ºC for 2 h FC	840	14.1
	SLM + (940 ºC for 1 h + 650 ºC for 2 h) after AC	948	13.6
This work	SLM	1261	9.8
	SLM+FSP at 400 rpm	**1085**	**19.9**

5. Conclusions

A selective laser melted (SLM) Ti6Al4V material has been successfully modified by friction stir processing (FSP). Detailed analysis of 3D X-ray microtomography and EBSD provide the following conclusions:

- FSP generates a homogeneous processed zones with the higher rotational speed of 400 rpm.
- The initial porosity (0.02 %) in the as-built sample is greatly supressed.
- The typical microstructure of α′ martensite laths inside columnar prior-β grains (SLMed sample) is replaced by α-plates, α-colonies and α-DRX inside equiaxed or semi-equiaxed prior-β grains decorated by GBα (FSPed sample).

An excellent combination of strength and ductility is achieved in this study. The mechanical characterizations lead to the following findings:

- Although UTS is slightly decreased from 1261 MPa to 1085 MPa, a very significant enhancement of fracture strain is obtained from 0.21 to 0.65.
- The fracture in the SLMed sample is controlled by plastic instability that develops among α′ laths, while the fracture in the FSPed sample is driven by ductile tearing from void coalescence.

As future work is concerned, FSP shows potential in enhancing the fatigue life of the SLMed Ti6Al4V alloy due to the reduction in large porosities that are known to be sources of premature fatigue crack nucleation.

Acknowledgements

C.J. Huang, L. Zhao and A. Simar acknowledge the financial support of the European Research Council for a Starting Grant under grant agreement 716678, ALUFIX project. X.C. Yan, M. Liu and W.Y Ma acknowledge the Guangdong Academy of Science Projects (2017GIFC008, 201807010030, and 2017A070701027). The author C.J.

Huang acknowledges A. Hilhorst and M. Lezaack for helps in the microhardness measurement, and also acknowledges Dr. Z.H. Zhang (Dongguan Jing Ming Metal Technology Co., Ltd. P.R. China), Prof. W.Y. Li (NPU, P.R. China) and Prof. H.L. Liao (UBFC, France) for support for experiments.

References:

[1]. D. Herzog, V. Seyda, E. Wycisk, C. Emmelmann, Additive Manufacturing of Metals, Acta Mater, 117 (2016) 371-92.

[2]. C.Y. Yap, C.K. Chua, Z.L. Dong, Z.H. Liu, D.Q. Zhang, L.E. Loh, S.L. Sing, Review of selective laser melting: Materials and applications, Appl Phys Rev, 2 (2015) 041101.

[3]. P. Wang, X.P. Tan, M.L.S. Nai, S.B. Tor, J. Wei, Spatial and geometrical-based characterization of microstructure and microhardness for an electron beam melted Ti-6Al-4V component, Mater Des, 95 (2016) 287-295.

[4]. T. Vilaro, C. Colin, J.D. Bartout, As-Fabricated and heat-treated microstructures of the Ti-6Al-4V alloy processed by selective laser melting, Met Mater Trans A, 42 (2011) 3190-3199.

[5]. G. Kasperovich, J. Hausmann, Improvement of fatigue resistance and ductility of TiAl6V4 processed by selective laser melting, J Mater Process Tech, 220 (2015) 202-214.

[6]. L. Thijs, F. Verhaeghe, T. Craeghs, J.V. Humbeeck, J.P. Kruth, A study of the microstructural evolution during selective laser melting of Ti-6Al-4V, Acta Mater, 58 (2010) 3303-3312.

[7]. X.C. Yan, S. Yin, C.Y. Chen, C.J. Huang, R. Bolot, R. Lupoi, M. Kuang, W.Y. Ma, C. Coddet, H.L. Liao, M. Liu, Effect of heat treatment on the phase transformation and mechanical properties of Ti6Al4V fabricated by selective laser melting, J Alloy Comp, 764 (2018) 1056-1071.

[8]. C.L. Qiu, N.J.E. Adkins, M.M. Attallah, Microstructure and tensile properties of selectively laser-melted and of HIPed laser-melted Ti-6Al-4V, Mater Sci Eng A, 578 (2013) 230-239.

[9]. W. Xu, E.W. Lui, A. Pateras, M. Qian, M. Brandt, In situ tailoring microstructure in additively manufactured Ti-6Al-4V for superior mechanical performance, Acta Mater, 125 (2017) 390-400.

[10]. S. Leuders, M. Thone, A. Riemer, T. Niendorf, T. Troster, H.A. Richard, H.J. Maier, On the mechanical behaviour of titanium alloy TiAl6V4 manufactured by selective laser melting: Fatigue resistance and crack growth performance, Int J Fatig, 48 (2013) 300-307.

[11]. B. Vrancken, L. Thijs, J.P. Kruth, J.V. Humbeeck, Heat treatment of Ti6Al4V produced by selective laser melting: microstructure and mechanical properties, J Alloy Comp, 541 (2012) 177-185.

[12]. V. Chastand, P. Quaegebeur, W. Maia, E. Charkaluk, Comparative study of fatigue properties of Ti-6Al-4V specimens built by electron beam melting (EBM) and selective laser melting (SLM), Mater Charact, 143 (2018) 76-81.

[13]. T. Persenot, A. Burr, G. Martin, J.Y. Buffiere, R. Dendievel, E. Mairea, Effect of build orientation on the fatigue properties of as-built Electron Beam Melted Ti-6Al-4V alloy, Int. J Fati, 118 (2019) 65-76.

[14]. M. Benedetti, E. Torresani, M. Leoni, V. Fontanari, M. Bandini, C. Pederzolli, C. Potrich, The effect of post-sintering treatments on the fatigue and biological behavior of Ti-6Al-4V ELI parts made by selective laser melting, J Mech Behav Biomed Mater, 71 (2017) 295-306.

[15]. R.S. Mishra, M.W. Mahoney, S.X. McFadden, N.A. Mara, A.K. Mukherjee, High strain rate superplasticity in a friction stir processed 7075 Al alloy, Scripta Mater, 42 (2000) 163-168.

[16]. Z.Y. Ma, S.R. Sharma, R.S. Mishra, Microstructural modification of as-cast Al-Si-Mg alloy by friction stir processing, Met Mater Trans A, 37 (2006) 3323-3335.

[17]. L. Karthikeyan, V.S. Senthilkumar, V. Balasubramanian, S. Natarajan, Mechanical property and microstructural changes during friction stir processing of cast aluminum 2285 alloy, Mater Des, 30 (2009) 2237-2242.

[18]. F. Hannard, S. Castin, E. Maire, R. Mokso, T. Pardoen, A. Simar, Ductilization of aluminium alloy 6056 by friction stir processing, Acta Mater, 2017 (130) 121-36.

[19]. S. Mironov, Y.S. Sato, H. Kokawa, Friction-stir welding and processing of Ti-6Al-4V titanium alloy: A review, J Mater Sci Tech, 34 (2018) 58-72.

[20]. J.Q. Su, J.Y. Wang, R.S. Mishra, R Xu, J.A. Baumann, Microstructure and mechanical properties of a friction stir processed Ti-6Al-4V alloy, Mater Sci Eng A, 573 (2013) 67-74.

[21]. J.G.S. Macias, J.Y. Buffière, E. Maire, J. Adrien, C. Elangeswaran, A. Cutolo, B.V. Hooreweder, F. Lani, P. Jacques, A. Simar. March 2018 Conference: EMMC16-16th European Mechanics of Materials Conference At: Nantes.

[22]. L. Zhou, H.J. Liu, Effect of 0.3 wt% hydrogen addition on the friction stir welding characteristics of Ti-6Al-4V alloy and mechanism of hydrogen-induced effect, Inter J Hyd Energy, 35 (2010) 8733-8741.

[23]. J.J. Yang, H.C. Yu, J. Yin, M. Gao, Z.M. Wang, X.Y. Zeng, Formation and control of martensite in Ti-6Al-4V alloy produced by selective laser melting, Mater Des, 108 (2016) 308-318.

[24]. S. Yoon, R.Ueji, H. Fujii, Effect of rotation rate on microstructure and texture evolution during friction stir welding of Ti-6Al-4V plates, Mater Character, 106 (2015) 352-358.

[25]. Y. Zhang, Y.S. Sato, H. Kokawa, S.H.C. Park, S. Hirano, Microstructural characteristics and mechanical properties of Ti-6Al-4V friction stir welds, Mater Sci Eng A, 485 (2008) 448-455.

[26]. Z.Y. Ma, A.L. Pilchak, M.C. Juhas, J.C. Williams, Microstructural refinement and property enhancement of cast light alloys via friction stir processing, Scripta Mater, 58 (2008) 361-366.

[27]. L. Lecarme, E.Maire, A.Kumar K.C., C.D, Vleeschouwer, L. Jacques, A. Simar, T. Pardoen, Heterogenous void growth revealed by in situ 3-D X-ray microtomography using automatic cavity tracking, Acta Mater, 2014 (63) 130-139.

[28]. H. Gong, K. Rafi, H. Gu, G.D. Janaki Ram, T. Starr, B. Stucker, Influence of defects on mechanical properties of Ti-6Al-4V components produced by selective laser melting and electron beam melting, Mater Des, 86 (2015) 545-554.

[29]. S. Biamino, A. Penna, U. Ackelid, S. Sabbadini, O. Tassa, P. Fino, M. Pavese, P. Gennaroe, C. Badin, Electron beam melting of Ti-48Al-2Cr-2Nb alloy: Microstructure and mechanical properties investigation, Intermet, 19 (2011) 776-781.

[30]. E.O. Olakanmi, R.F. Cochrane, K.W. Dalgarno, A review on selective laser sintering/melting (SLS/SLM) of aluminium alloy powders: Processing, microstructure, and properties, Pro Mater Sci, 74 (2015) 401-477.

[31]. Y.M. Ren, X. Lin, X. Fu, H. Tan, J. Chen, W.D. Huang, Microstructure and deformation behavior of Ti-6Al-4V alloy by high-power laser solid forming, Acta Mater, 125 (2017) 390-400.

[32]. B.E. Carroll, T.A. Palmera, A.M. Beese, Anisotropic tensile behavior of Ti-6Al-V components fabricated with directed energy deposition additive manufacturing, Acta Mater, 87 (2015) 309-320.

[33]. A. Simar, Y. Bréchet, B. de Meester, A. Denquin, C. Gallais, T. Pardoen, Integrated modeling of friction stir welding of 6xxx series Al alloys: Process, microstructure and properties, Pro Mater Sci, 57 (2012) 95-183.

[34]. N. Hansen, Hall-Petch relation and boundary strengthening, Scripta Mater, 51 (2004) 801-806.